Merging galaxy clusters: probing magnetism and particle acceleration over cosmic time

Di Gennaro, G.

CHAPTER

4

FAST MAGNETIC FIELD AMPLIFICATION IN DISTANT GALAXY CLUSTERS

G. Di Gennaro, R.J. van Weeren, G. Brunetti, R. Cassano, M. Brüggen et al. *Nature Astronomy*, 5, 268 (2021)

Abstract. The origin and the amplification of magnetic fields during structure formation is still not understood. We report Low Frequency Array (LOFAR) observations, which reveal large-scale diffuse radio emission from galaxy clusters when the Universe was only half of its present age (i.e. $z > 0.6$). The observed synchrotron emission indicates the existence of cosmic rays and magnetic field, associated with the dilute intracluster medium. We find that the diffuse radio emission in massive, distant clusters is common, and the high radio luminosities, in spite of the strong Inverse Compton losses at high redshifts, indicates that these clusters have magnetic field strengths that are similar to those in nearby clusters. This implies that magnetic field amplification during the first phases of cluster formation is fast, which has strong implications for models of magnetogenesis.

In the present-day Universe, magnetic fields pervade galaxy clusters (Carilli & Taylor, 2002), with strengths of a few microGauss obtained from Faraday Rotation (Bonafede et al., 2010a). Evidence for cluster magnetic fields is also provided by Megaparsec-scale radio emission, namely radio halos and relics (van Weeren et al., 2019). These are commonly found in merging systems (Cassano et al., 2010b) and are characterized by a steep radio spectrum ($\alpha < -1$, where $S_\nu \propto \nu^\alpha$). It is widely believed that magneto-hydrodynamical turbulence and shock-waves (re-)accelerate cosmic rays (Brunetti & Jones, 2014), producing halos and relics. The origin and the amplification of magnetic fields in clusters is not well understood. It has been proposed that turbulence drives a small-scale dynamo (Dolag et al., 2005; Subramanian et al., 2006; Ryu et al., 2008; Miniati & Beresnyak, 2015; Vazza et al., 2018; Domínguez-Fernández et al., 2019) that amplifies seed magnetic fields (primordial and/or injected by galactic outflows, as active galactic nuclei, starbursts, or winds; Donnert et al., 2018). At high redshift, radio halos are expected to be faint, due to the Inverse Compton losses and dimming effect with distance. Moreover, Faraday Rotation measurements are difficult to obtain. If detected, distant radio halos provide an alternative tool to investigate magnetic field amplification. Here, we report LOFAR observations which reveal diffuse radio emission in massive clusters when the Universe was only half of its present age, with a sample occurrence fraction of about 50%. The high radio luminosities indicate that these clusters have similar magnetic field strengths to those in nearby clusters, and suggest that magnetic field amplification is fast during the first phases of cluster formation.

To investigate this unexplored territory, we present a systematic investigation of magnetic fields in distant galaxy clusters, using the low-frequency radio telescope LOFAR (van Haarlem et al., 2013). Our observations were taken from the LOFAR Two-metre Sky Survey (LoTSS; Shimwell et al., 2019). The 120–168 MHz LoTSS survey has a spatial resolution of approximately 6″ and reaches a median sensitivity of about 70 μJy beam^{-1} (Shimwell et al., 2019). Currently, LoTSS covers about 40% of the Northern sky. The clusters were selected from the latest *Planck* Sunyaev-Zel'dovich (SZ) PSZ2 catalog (Planck Collaboration et al., 2016), at redshift above 0.6 and declination above 20 degrees. The advantage of SZ-selection is that the SZ-signal ($y \propto \int n_e T_e dl$, i.e. the line of sight integral of the product of the electron number density, n_e, and the electron temperature, T_e) does not suffer from redshift dimming and the integrated cluster's SZ-signal is closely related to the cluster mass ($M_{\rm SZ,500}$). The cluster masses are taken from the *Planck* catalog, and are obtained from the integrated cluster's SZ-signal within R_{500}, where R_{500} is the radius with a density 500 times the critical density of the Universe at the given redshift.

Using this selection and taking the available LoTSS observations, we obtain a sample of 19 galaxy clusters in a redshift range of $\sim 0.6 - 0.9$ and with masses $M_{\rm SZ,500} \sim 4 - 8 \times 10^{14}$ M$_\odot$. These objects are among

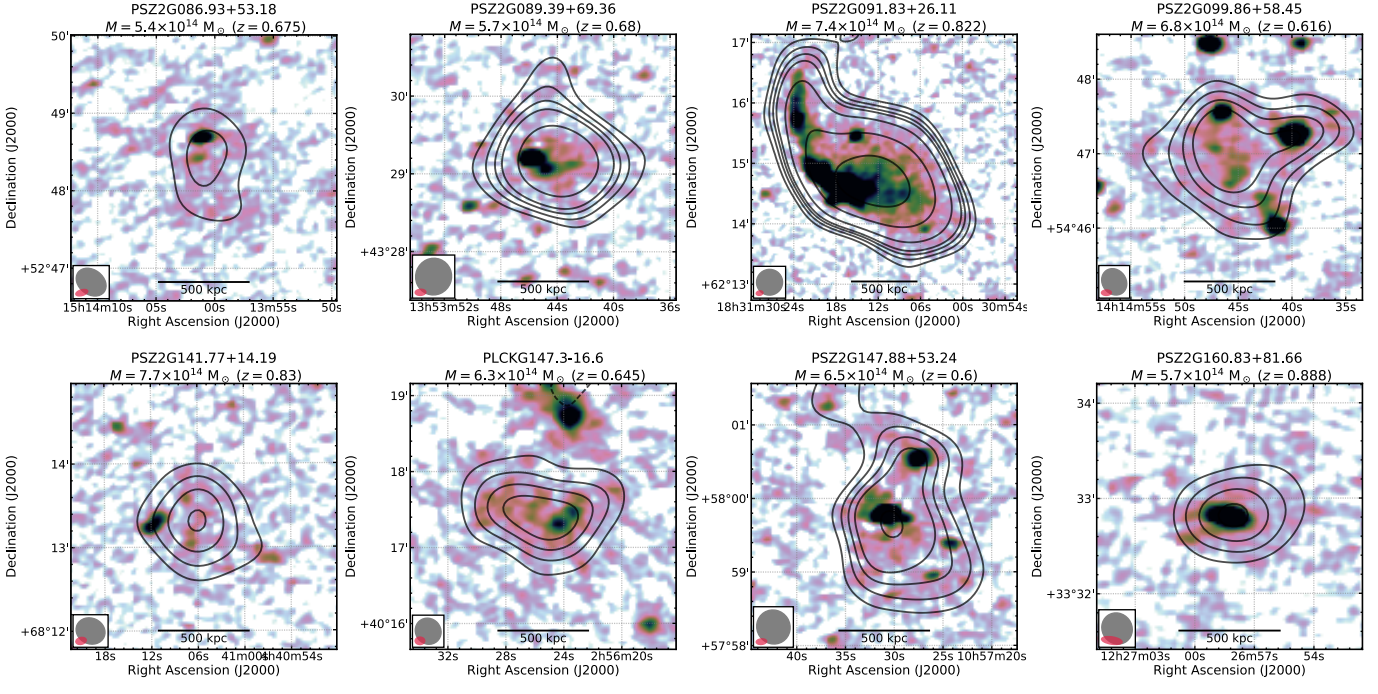

Figure 4.1: Examples of observed radio emission in our high-z galaxy cluster sample. In colorscale we show the full-resolution LOFAR images, while radio contours show the low-resolution emission after the subtraction of compact sources, displayed at the $[-2, 2, 3, 4, 5, 8, 16]\times\sigma_{\rm rms}$ level (with $\sigma_{\rm rms}$ the individual map noise; the negative contour levels are indicated with a short-dashed line style). The full- and low-resolution LOFAR beams are displayed in the bottom left corner (in pink and grey colors, respectively). In the header of each image, the galaxy cluster name, mass and redshift are reported.

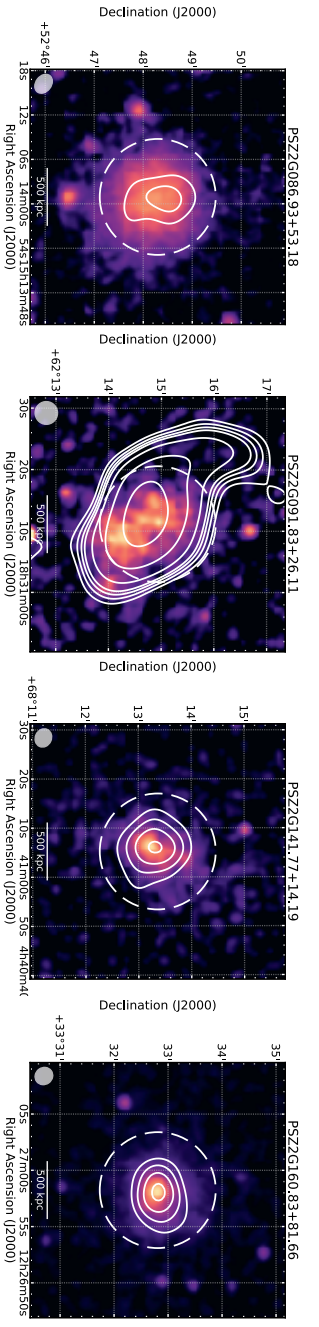

Figure 4.2: X-ray images of a sub-sample of Figure 1. LOFAR radio contours are drawn as Figure 1, with the LOFAR beam displayed in the bottom left corner. The dashed white circle in each map shows the $R = 0.5R_{SZ,500}$ region, obtained from $M_{SZ,500}$. In the header of each image, the galaxy cluster name is reported.

the most massive structures at these redshifts. In Figure 4.1, we show a number of full-resolution (i.e. about 6″) LOFAR images of the detected diffuse radio sources from our sample, with radio contours tracing the low-resolution (approximately 15″) emission, without compact sources (for the full sample, see Figure 4.4). We find that at least nine out of the 19 clusters host diffuse radio emission (see Table 4.1). The diffuse emission is mostly centrally located in the clusters, with an overall roundish shape, and extending over scales spanning from few hundreds of kiloparsec to about one Megaparsec. In those systems that have targeted X-ray observations, the radio emission follows the thermal radiation, see Figure 4.2 (for the full sample, see Figure 4.5). We therefore classify these diffuse sources as radio halos. From the X-ray images, most clusters look dynamically disturbed. Particularly noteworthy among the clusters in our sample are PSZ2 G091.83+26.11 at $z = 0.822$, where a very bright Megaparsec-sized radio halo and relic are present, and PSZ2 G160.83+81.66 at $z = 0.888$, which hosts the most distant radio halo discovered to date, with a size of 0.7 Mpc.

Based on the radio flux density measurements and assuming $\alpha = -1.5 \pm 0.3$, we compute radio luminosities in the range $P_{1.4\mathrm{GHz}} \sim 0.7 - 14 \times 10^{24}$ W Hz^{-1} (Table 4.1). Although most of the radiation in high-redshift halos is expected to be emitted via Inverse Compton (IC), the radio luminosities of these halos fall surprisingly within the scatter of those observed in nearby (median value $z \sim 0.2$ Cassano et al., 2013) galaxy clusters of the same mass range (see Figure 4.3a).

For synchrotron emission, the similar radio luminosities imply that the product of the number of the radio-emitting electrons and magnetic field ($N_e \times B^2$) in high-redshift clusters is similar to that in lower-redshift systems of comparable mass. Furthermore, this key observable may also suggests that both the magnetic field strength and the number of electrons in high-redshift clusters are comparable to those in low-z systems, otherwise the energetics of the halos would be very different while generating similar radio luminosities.

In re-acceleration models, the synchrotron luminosity is (Cassano et al., 2019; Brunetti & Vazza, 2020)

$$P_{\mathrm{rad}} \propto \eta_{\mathrm{rel}} \frac{\rho v_t^3}{L_{\mathrm{inj}}} \frac{B^2}{B^2 + B_{\mathrm{CMB}}^2}\,, \tag{4.1}$$

where $\rho v_t^3 / L_{\mathrm{inj}}$ is the turbulent energy flux (with ρ the gas density, and v_t and L_{inj} the turbulent velocity and injection scale, respectively), η_{rel} is the fraction of the turbulent energy flux that is dissipated in the re-acceleration of seed relativistic electrons, B is the magnetic field averaged over the halo volume and $B_{\mathrm{CMB}} = 3.25(1+z)^2$ μG is the CMB equivalent magnetic field strength. The ratio $\frac{B^2}{B^2+B_{\mathrm{CMB}}^2}$ sets the fraction of non-thermal luminosity that is emitted into synchrotron radiation. The stronger en-

Table 4.1: Integrated flux density and radio luminosity of the galaxy clusters observed with LOFAR. Column 1: *Planck* cluster name. Column 2: Cluster redshift. Column 3: Largest linear size (LLS) of the diffuse radio emission. Column 4: Classification of the diffuse radio emission. Column 5: Integrated flux density of the diffuse emission (compact sources removed). Column 6: 1.4 GHz (k-corrected) radio luminosity.

Planck (PSZ) name	z	LLS [Mpc]	Classification	$S_{144\mathrm{MHz}}$ [mJy]	$P_{1.4\mathrm{GHz}}$ [10^{24} W Hz^{-1}]
PSZ2G045.87+57.70	0.611	–	Uncertain	–	–
PSZ2G070.89+49.26	0.610	–	–	–	–
PSZ2G084.10+58.72	0.731	–	Uncertain	–	–
PSZ2G086.28+74.76	0.699	–	Uncertain	–	–
PSZ2G086.93+53.18	0.675	0.5	Halo	7.2 ± 1.5	0.7 ± 0.4
PSZ2G087.39+50.92	0.748	–	–	–	–
PSZ2G089.39+69.36	0.680	1.0	Halo	12.5 ± 1.9	1.3 ± 0.7
PSZ2G091.83+26.11	0.822	1.2	Halo	84.3 ± 12.7	13.8 ± 8.4
		1.2	Relic	259.4 ± 38.9	–
PSZ2G092.69+59.92	0.848	–	–	–	–
PSZ2G099.86+58.45	0.616	1.2	Halo	27.8 ± 4.3	2.2 ± 1.3
PSZ2G104.74+40.42	0.690	–	Uncertain	–	–
PSZ2G126.28+65.62	0.820	0.8	Halo	8.8 ± 1.7	1.4 ± 0.6
PSZ2G127.01+26.21	0.630	–	Uncertain	–	–
PSZ2G139.00+50.92	0.600	–	–	–	–
PSZ2G141.77+14.19	0.830	0.6	Halo	8.8 ± 1.4	1.4 ± 0.7
PSZ2G141.98+69.31	0.714	–	–	–	–
PLCKG147.3–16.6	0.645	0.8	Halo	22.5 ± 3.7	$6.4 \pm 3.4^{\star}$
PSZ2G147.88+53.24	0.600	0.6	Halo	14.4 ± 2.3	0.9 ± 0.5
PSZ2G160.83+81.66	0.888	0.7	Halo	13.0 ± 2.1	2.7 ± 1.5

Note: Uncertainties on the 1.4 GHz radio luminosity include the flux density and spectral index uncertainties, assuming a Gaussian distribution of spectral indices ($\alpha = -1.5 \pm 0.3$), see Method. *We used the spectral index obtained combining our LOFAR observation with literature GRMT flux measurement (van Weeren et al., 2014, see the Supplementary).

ergy losses due to IC ($dE/dt \propto (1+z)^4$) are expected to balance the effect of a potentially larger injection rate of electrons at higher redshift (due to enhanced activity of active galactic nuclei and/or star-forming galaxies). For this reason we can assume that the budget of seed particles that accumulate in the ICM at high redshift is similar to that at lower redshift (as detailed in the Methods). For a fixed budget of seed particles to re-accelerate, η_{rel} depends only on the interplay between turbulence and particles Brunetti & Jones (2014), and we assume it is independent of redshift. From the comparison of their radio luminosities, and taking into account that mergers at $z \sim 0.7 - 0.8$ generate more turbulent energy flux compared to the $z = 0.2$ sample (by a factor ~ 3, see Methods), we find

that the magnetic field in high-z halos has to be similar to that observed for local clusters, i.e. $B \geq 1$ μG. This suggests that the magnetic field amplification has been surprisingly efficient, producing a microGauss-level field in a Mpc^3 volume already at $z \sim 0.7$, i.e. within few Gyr from cluster formation (see Figure 4.3b). This result provides important insights on the origin and evolution of magnetic fields in galaxy clusters.

It is widely accepted that the small-scale turbulent dynamo plays a role in the amplification of the initial magnetic field from primordial seeds or galactic outflows (Donnert et al., 2018). Initially, the amplification operates in a kinematic regime, where the magnetic field grows exponentially with time ($B^2(t) \sim B_0^2 \exp(t\,\Gamma)$). The competition of turbulent stretching and diffusion makes this phase initially very slow, with a growth time-scale $\Gamma^{-1} = 30 L_{\rm inj}/({\rm Re}^{1/2} v_t)$ (Cho, 2014; Beresnyak & Miniati, 2016), where Re is the Reynolds number. When the magnetic and the kinetic energy densities become comparable at the viscous dissipation scale, the turbulent dynamo becomes faster and transits to a phase where the magnetic field grows linearly with time. During this phase, the magnetic field reaches equipartition with the kinetic turbulent energy at increasingly larger scales, and saturates after several eddy turnover times (several Gyrs). In this scenario, our observations then require a fast magnetic amplification during the initial exponential phase, as it needs to be much shorter than a few Gyrs. This constrains the initial field and the ICM Reynolds number, being ${\rm Re} > 4 \times 10^4$ and $> 5 \times 10^3$ for $B_0 \sim 1$ nG and ~ 0.1 μG, respectively, assuming a continuous injection of turbulence with $v_t = 500$ km s^{-1} at the injection scale $L_{\rm inj} = 1$ Mpc (Dolag et al., 2005; Donnert et al., 2018; Hitomi Collaboration et al., 2018), the ICM number density of $n = 3 \times 10^{-3}$ cm^{-3} (Markevitch & Vikhlinin, 2007), and a time available for the magnetic field amplification of ~ 3.7 Gyr (see Figure 4.3b and Methods). These values of the Reynolds number are much larger than the classical value obtained assuming Coulomb collisions (≈ 100; Brunetti & Lazarian, 2007; Cho, 2014), and would suggest that kinetic effects and instabilities play an important role in the weakly-collisional magnetized ICM (Schekochihin & Cowley, 2006). This is also in line with recent X-ray observations in the ICM of local systems that have suggested a much smaller viscosity than the isotropic value obtained only considering Coulomb collisions (Zhuravleva et al., 2019). In case of a smaller Reynolds number, our observations would require that the activity of galactic outflows and AGN in high redshift clusters is sufficient to generate microGauss fields spread on > 100 kpc scales (Xu et al., 2011). This would generate a clumpier distribution of the radio emission in the cluster volume. This can be tested with deeper observations, in combination with predictions of the spatial distribution of radio emission from cosmological magneto-hydrodynamic simulations that explore different magnetogenesis scenarios.

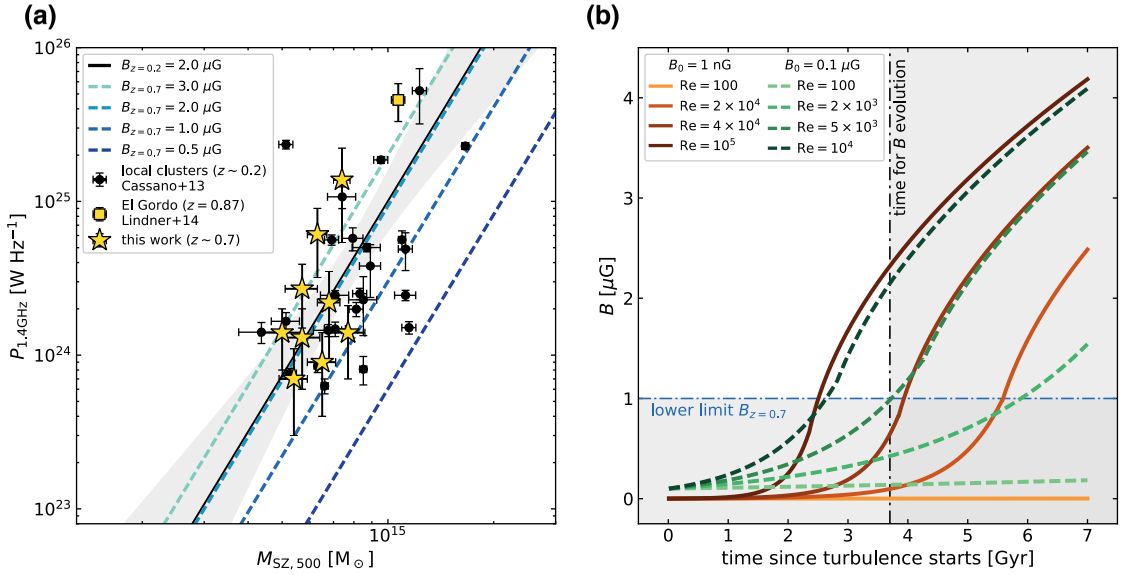

Figure 4.3: Cluster magnetic field estimation and theoretical magnetic field evolution. *Panel (a):* $P_{1.4\mathrm{GHz}}$–M_{500} diagram for nearby ($median(z) \sim 0.2$, black dots Cassano et al., 2013) and distant ($median(z) \sim 0.7$, yellow starts) radio halos, including that in El Gordo ($z = 0.87$, Lindner et al., 2014, yellow square). Error bars on the yellow stars are obtained with 100 Monte Carlo realization of the radio luminosity, including flux density and spectral index uncertainties, while error bars on the black dots and yellow square are given by the literature. The black solid line represents the best-fit relation from the low-redshift sample, with the 95% level confidence (grey area). The blue dashed lines represent, from light to darker colors, the theoretical relations at high-z taking magnetic field strengths of 3.0, 2.0, 1.0 and 0.5 μG (assuming a typical local cluster magnetic field of 2 μG). *Panel (b):* Magnetic field growth since the start of the turbulence, based on the small-scale dynamo theory. The initial fields, B_0, are set at 1 nG (solid orange lines; from light to darker colors: Re = [100, 2×10^4, 4×10^4, 10^5]) and 0.1 μG (dashed green lines; from light to darker colors: Re = [100, 2×10^3, 5×10^3, 10^4]). The horizontal blue dot-dashed line sets the lower limit of the magnetic field strength in distant galaxy clusters (see panel *(a)*). The vertical black dot-dashed line shows the upper limit on the approximate time available for the magnetic field growth (see Methods).

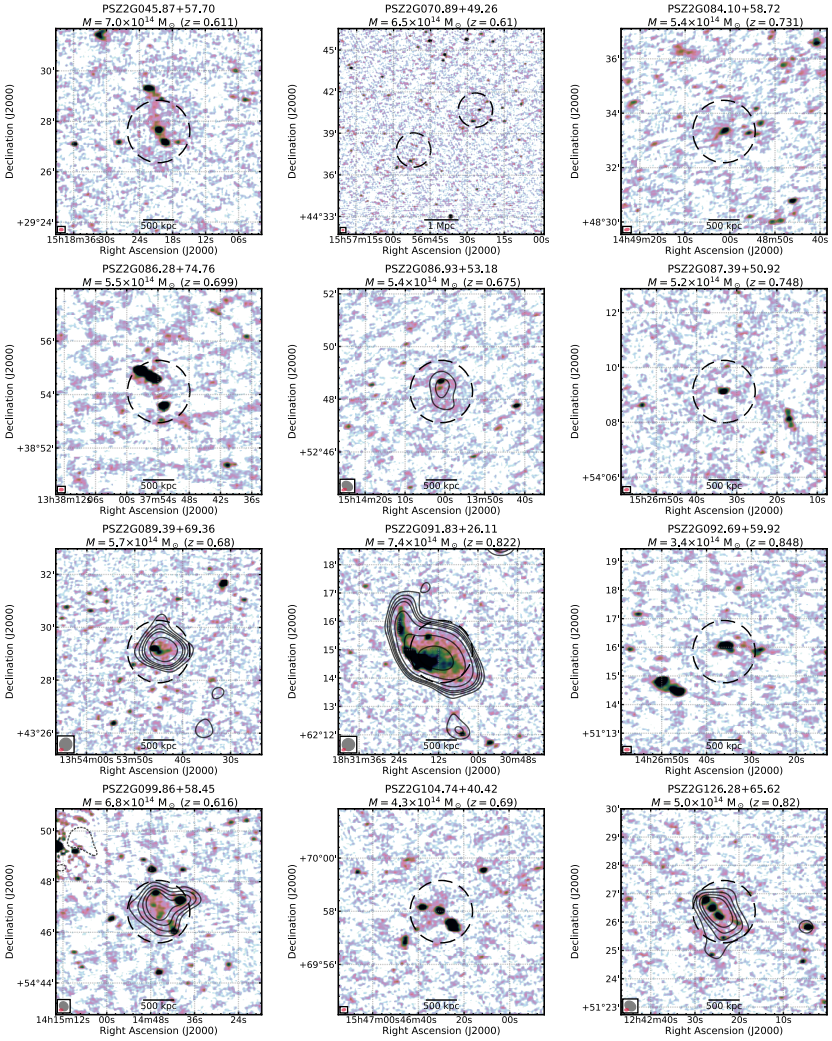

Figure 4.4: Observed radio emission in our high-z galaxy cluster sample. In colorscale we show the full-resolution LOFAR images. Low-resolution source-subtracted radio contours, displayed at the $[-2, 2, 3, 4, 5, 8, 16] \times \sigma_{\rm rsm}$ level, are shown only for clusters that host diffuse radio emission (with $\sigma_{\rm rsm}$ the individual map noise; the negative contour levels are indicated with a short-dashed line style). The full- and low-resolution LOFAR beams are displayed in the bottom left corner (in pink and grey colors, respectively). In the header of each image, the galaxy cluster name, mass and redshift are reported. The dashed black circle in each map shows the $R = 0.5 R_{\rm SZ,500}$ region, obtained from $M_{\rm SZ,500}$.

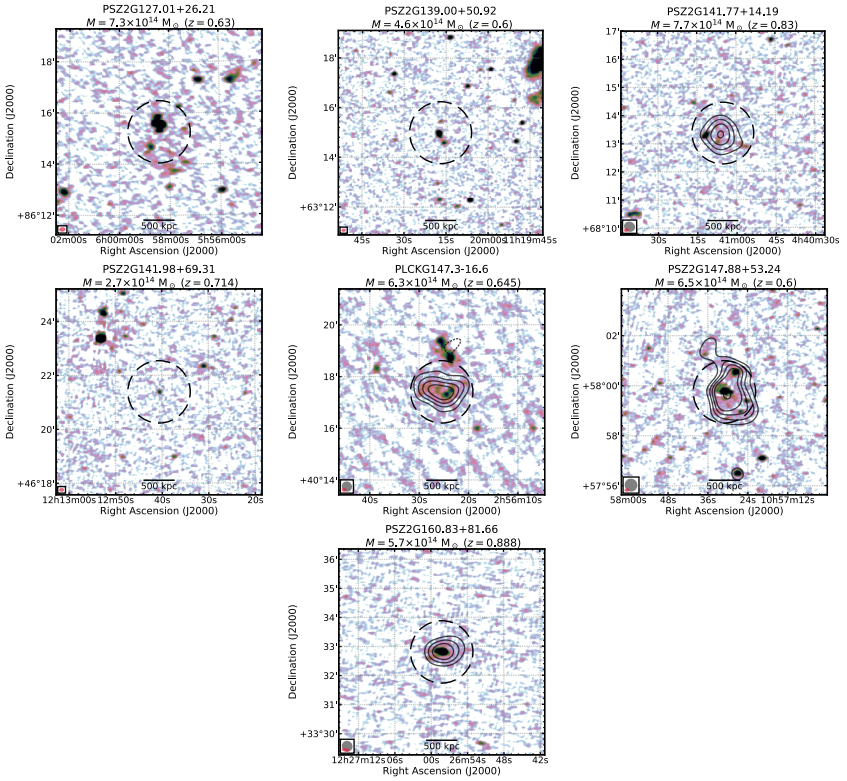

Figure 4.4: Continued

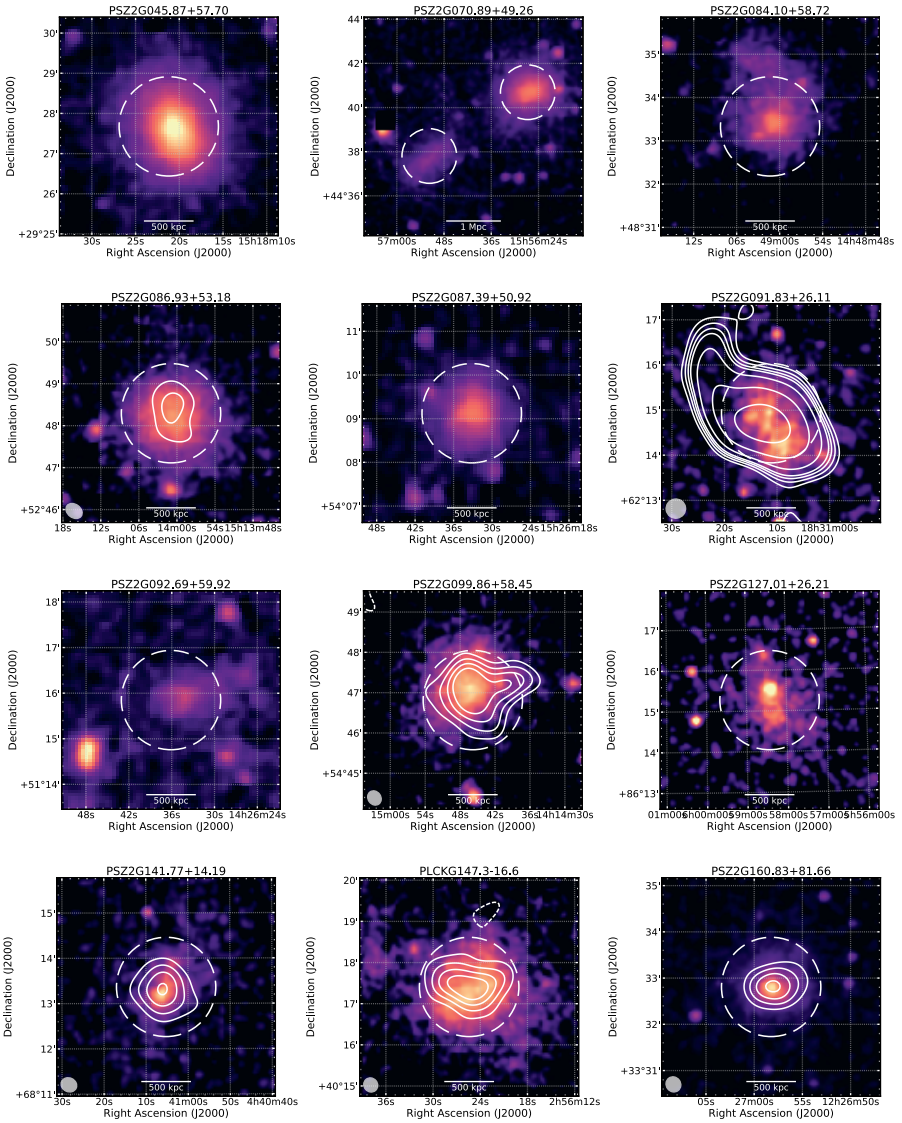

Figure 4.5: X-ray images of all the galaxy clusters in our sample. In colorscale we show the *Chandra*/*XMM-Newton* images. LOFAR radio contours are drawn as Figure 1, with the LOFAR beam displayed in the bottom left corner. The dashed white circle in each map shows the $R = 0.5R_{SZ,500}$ region, obtained from $M_{SZ,500}$. In the header of each image, the galaxy cluster name is reported.

4.1. Methods

Galaxy cluster sample selection

We construct our sample of high-z galaxy clusters using the latest *Planck* Sunyaev-Zel'dovich (SZ) catalog, i.e. PSZ2 (Planck Collaboration et al., 2016). This catalog provides a reliable cluster mass estimation for galaxy clusters up to $z \sim 1$. Although the exact effect of selection biases is still being debated and may overestimate the observed fraction of clusters with radio halos, there is no clear consensus in the literature that suggests the SZ sample chosen here disproportionately favours merging over relaxed clusters (Eckert et al., 2011; Rossetti et al., 2017; Andrade-Santos et al., 2017). We select all the objects at DEC $\geq 20°$, to match the part of the sky with the best LOFAR sensitivity, and $z \geq 0.6$. No mass-threshold has been applied in our cluster selection. These selection criteria result in a sample of 30 objects (see Table 4.2 in the Supplementary). The sample includes clusters where precise redshift measurements became available recently (van der Burg et al., 2016; Amodeo et al., 2018; Barrena et al., 2018; Burenin et al., 2018; Sereno et al., 2018; Streblyanska et al., 2018; Zohren et al., 2019) and a previous-discovered *Planck* cluster, i.e. PLCK G147.3–16.6 (van Weeren et al., 2014). We used the optical images from the Panoramic Survey Telescope and Rapid Response System (Pan-STARRS; Chambers et al., 2016) to refine the accuracy of the cluster center coordinates, using the brightest cluster galaxy (BCG), when detected, or approximately the center of the distribution of the galaxies. We also inspected the *Chandra* and/or *XMM-Newton* X-ray image, when available, to verify the correspondence of the cluster coordinates with the center of the thermal gas distribution. Among these 30 *Planck* clusters, 21 objects were already covered as part of the LOFAR Two-metre Sky Survey (LoTSS; Shimwell et al., 2019). From these 21 clusters one was affected by bad ionospheric observing conditions (i.e. PSZ2 G088.98+55.07) and one lays on the same line of sight of a cluster at $z = 0.3$ (i.e. PSZ2 G097.52+51.70). Those are therefore excluded from the final sample (see Figure 4.4), consisting of 19 objects at median redshift of $z = 0.7$.

LOFAR observations, data reduction, images and flux measurements

The LOFAR observations were carried out together with the LOFAR Two-metre Sky Survey (LoTSS; Shimwell et al., 2019) in the 120–168 MHz frequency range. The survey consists in 8 hours of observation for each pointing, with a field of view of $\sim 2.6°$, full resolution of about $6''$, and median noise of about 70 μJy beam^{-1}. Given the large sky coverage already achieved by the survey, our targets were often observed by more than one

pointing (see Table 4.3 in the Supplementary), which further improved our signal to noise. For each LoTSS pointing, we performed standard data reduction Shimwell et al. (2019), which includes direction-independent and dependent calibration, and imaging of the full LOFAR field of view using `prefactor` (van Weeren et al., 2016; Williams et al., 2016; de Gasperin et al., 2019), `killMS` (Tasse, 2014; Smirnov & Tasse, 2015) and `DDFacet` (Tasse et al., 2018). We additionally improved the quality of the calibration, using the products of the pipeline, subtracting all the sources outside a region of $\sim 15' \times 15'$ surrounding the target, and performing extra phase and amplitude self-calibration loops in each target sub-field. To verify the quality of the calibration, each pointing is imaged independently using `WSClean` (Offringa et al., 2014), with the wideband deconvolution mode (`channelsout=6`). For all our imaging, we employ automatic clean masks for the deconvolution. We utilize a $3\sigma_{\rm rms}$ masking threshold, with $\sigma_{\rm rms}$ the local map noise, and cleaning down to the $1\sigma_{\rm rms}$ level inside the mask. The images have a central frequency of 144 MHz, and are provided in the Figure 4.4.

All the clusters in our sample were carefully visually inspected in the full-resolution image to search for extended radio emission. To emphasize the presence of diffuse radio emission, we also produced low-resolution source-subtracted images. We first applied an uv-cut to the data, to filter out emission associated to linear sizes larger than 500 kiloparsecat the cluster redshift and to create a clean component model of the compact sources. For PSZ2 G089.39+69.36 we apply an uv-cut corresponding to 400 kpc. During this step, we employed multiscale deconvolution (Offringa & Smirnov, 2017), using scales of $[0, 4, 8, 16] \times$ pixelscale (with the pixel size of $1.5''$) to properly include and subtract somewhat extended radio galaxies. In addition, for the automatic deconvolution we lower the mask threshold to $1\sigma_{\rm rms}$ to subtract the faintest contaminating sources (see Supplementary Figure 4.6). Finally, we subtracted the compact sources model from the visibilities and tapered the uv-data to $\sim 15''$ resolution. It is important to note that in case of an extended radio galaxy, with linear size $\gtrsim 500$ kpc, this method cannot properly subtract the radio emission from the uv-data. For that reason, the extended double-lobed radio galaxy just north of PLCKG147.3–16.6 has been manually excluded and blanked in the low-resolution source-subtracted image (Figures 4.1 and 4.4).

We used these low-resolution source-subtracted images to define the largest linear size (LLS) of the diffuse radio emission, following the $2\sigma_{\rm rms}$ contour. Systems with LLS < 500 kpc were not included in our statistics. Roundish, centrally-located significantly detected sources (see the next paragraph) that follow the ICM distribution were classified as radio halos; elongated, peripheral structures were classified as radio relics. We did not identify clear examples of fossil radio plasma sources (i.e. "radio phoenices"), these typically have small sizes (i.e. 200 kpc or smaller), irregular shapes, and are not centered on the cluster center (de Gasperin

et al., 2017; Mandal et al., 2020). Similarly, we did not find clear examples of "mini-halos", as these diffuse sources usually have LLS smaller than 500 kpc and are located in dynamically relaxed systems (Giacintucci et al., 2017). Uncertain classifications, due to contamination from extended radio galaxies in the cluster region and/or ambiguous shapes, were excluded from our final statistical analysis. If we measure the LLS following the $3\sigma_{\rm rms}$ contour, we would classify 8 radio halos instead of 9 (see Table 4.4 in the Supplementary).

To determine the integrated flux densities for the radio halos, we first measured the total cluster radio flux densities (i.e. compact sources and diffuse emission) from the low-resolution image, following the $2\sigma_{\rm rms}$ radio contour to fully cover the extension of the diffuse radio emission (see Figure 4.4). In Table 4.4, we also report the integrated flux density measurements following the $3\sigma_{\rm rms}$ radio contour. We then mathematically subtracted the flux densities of the compact sources within the cluster region, measured in the full-resolution uv-cut image, to obtain the flux density associated to the diffuse radio sources (Cassano et al., 2019). For PSZ2 G091.83+21.16, which also hosts a bright radio relic, we visually separated it from the radio halo region (see Figure 4.6 in the Supplementary). The uncertainties on the flux densities are estimated adding in quadrature the $\sigma_{\rm rms}$ statistical uncertainty, the 15% systematic error associated to the LOFAR flux scale calibration, $f_{\rm cal}$ (Shimwell et al., 2019), and the uncertainty due to the source subtraction in the cluster region, $\sigma_{\rm sub}$ (Cassano et al., 2013), according the following Equation:

$$\Delta S = \sqrt{(f_{\rm cal} S_{144\rm MHz})^2 + \sigma^2_{\rm rms} N_{\rm beam,h} + \sigma^2_{\rm sub}}\,. \tag{4.2}$$

Here, $\sigma^2_{\rm sub} = \sum_i \sigma^2_{\rm rms} N_{\rm beam,s_i}$, and $N_{\rm beam,h}$ and $N_{\rm beam,s_i}$ are the number of beams covering the halo and the subtracted i sources, respectively. Uncertainties associated to possibly missed faint compact sources are not included, but these should be smaller than the systematic error associated to the LOFAR flux scale calibration.

We confirmed the presence of diffuse radio emission when the measured integrated radio flux density is larger than five times the flux uncertainty, i.e. $\frac{S_{144\rm MHz}}{\Delta S} \geq 5$ (see Column 5 in Table 4.1). Flux density measurements directly obtained from the low-resolution source-subtracted images are also provided in the Supplementary.

Finally, we calculated the k-corrected radio luminosity at 1.4 GHz:

$$P_{1.4\rm GHz} = 4\pi D_L^2 \frac{S_{1.4\rm GHz}}{(1+z)^{\alpha+1}}\,, \tag{4.3}$$

with D_L the luminosity distance assuming standard ΛCDM cosmology (i.e. $H_0 = 70$ km s^{-1} Mpc^{-1}, $\Omega_m = 0.3$, and $\Omega_\Lambda = 0.7$) and $S_{1.4\rm GHz} = S_{144\rm MHz}\left(\frac{1.4\rm GHz}{144\rm MHz}\right)^{\alpha}$. Since the spectral indices of the radio halos are not

measured, we assume a Gaussian distribution of spectral indices α with mean value −1.5 and scatter 0.3 for computing the radio luminosity. These values were chosen to encompass the typical range of spectral indices found in radio halos (van Weeren et al., 2019), and to take into account that they could be steeper than local systems (Cassano et al., 2006). Only for PLCK G147.3–16.6, we used the spectral index obtained combining our observations with the GMRT literature data (van Weeren et al., 2014, see Supplementary). The radio luminosities are listed in Table 4.1, whose uncertainties are obtained by performing Monte Carlo simulations including the flux density uncertainties and the spectral index uncertainty.

X-ray observations and data reduction

Twelve clusters among our LOFAR sample have also *Chandra* and/or *XMM-Newton* observations (see Figure 4.5 and Table 4.5 in the Supplementary).

Chandra data were reduced using the `chav` software package (`http://hea-www.harvard.edu/~alexey/CHAV/`) with `CIAO v4.6` and applying the `CALDB v4.7.6` calibration files (Vikhlinin et al., 2005). The processing includes the application of gain maps to calibrate photon energies, filtering out counts with ASCA grade 1, 5, or 7 and bad pixels, and a correction for the position-dependent charge transfer inefficiency (CTI). Periods with count rates with a factor of 1.2 above and 0.8 below the mean count rate in the 6–12 keV band were also removed. Standard blank-sky files were used for background subtraction. The final exposure-corrected images were made in the 0.5–2.0 keV band using a pixel binning of a factor of 4 (i.e 2″) and combining the different ObsIDs together where relevant (i.e., PSZ2 G160.83+81.66).

XMM-Newton observations were reduced using version 17.0.0 of the dedicated Science Analysis System (SAS). After converting the observation data files to unfiltered event lists, we extracted light curves in bins of 100 seconds in the energy ranges 10–12 keV for the MOS and 10–14 keV for the pn detectors onboard. Good time intervals were created excluding periods when the mean count rates in these light curves were different from the corresponding mean by more than 2 standard deviations. Images were extracted in the 0.4–7.0 keV band, using only the highest quality (FLAG==0) single to quadruple MOS events (PATTERN≤12) and single to double pn events (PATTERN≤4). Images were weighted by the respective exposure maps for each detector and combined, accounting for a factor ~2.5 difference between the typical expected count rates for MOS and pn at a given source flux (due to the slightly different effective areas and the fact that the light focused by two of the XMM-Newton telescopes is split evenly between the MOS and RGS detectors). Since we are interested mostly in the morphology of high-redshift, thus relatively compact, clusters positioned

close to the aim point, the effects of vignetting and instrumental particle background are minimal and have not been corrected for this analysis.

Turbulent energy flux at high redshift

According to re-acceleration models, relativistic electrons in radio halos are re-accelerated by turbulence. Assuming that turbulence in the ICM is mainly injected by cluster mergers, then the turbulence injection rate is $\rho v_i^3/L_{\rm inj}$ (Cassano & Brunetti, 2005), with v_i the impact velocity between the two merging clusters, ρ the cluster mean density and $L_{\rm inj}$ the injection scale of turbulence (which can be assumed to be of the same order of the cluster size, about 1 Mpc at both $z = 0.2$ and $z = 0.7$). The relative impact velocity of two subclusters with virial masses M_v and ΔM_v which collide (at a distance R_v between the centers) starting from an initial distance d_0 with zero velocity is given by Sarazin (2002):

$$v_i \simeq \sqrt{2G\frac{(M_v + \Delta M_v)}{R_v}\left(1 - \frac{1}{\eta_v}\right)}. \tag{4.4}$$

Here, $d_0 = \eta_v R_v$, $\eta_v \simeq 4\left(\frac{M_v+\Delta M}{M_v}\right)^{1/3}$, and R_v is the virial radius of the main cluster, i.e., the radius at which the ratio between the average density in the cluster and the mean cosmic density at the redshift of the cluster is given by Kitayama & Suto (1996):

$$\Delta_c(z) = 18\pi^2(1 + 0.4093\,\omega(z)^{0.9052}), \tag{4.5}$$

where $\omega(z) \equiv \Omega_f(z)^{-1} - 1$ with:

$$\Omega_f(z) = \frac{\Omega_{m,0}(1+z)^3}{\Omega_{m,0}(1+z)^3 + \Omega_\Lambda}. \tag{4.6}$$

The virial mass, M_v, and the virial radius are thus related by:

$$R_v = \left[\frac{3M_v}{4\pi\Delta_c(z)\rho_m(z)}\right]^{1/3} \tag{4.7}$$

where $\rho_m(z) = 2.78{\times}10^{11}\,\Omega_{m,0}\,(1{+}z)^3\,h^2\,{\rm M}_\odot\,{\rm Mpc}^{-3}$ is the mean mass density of the Universe at redshift z. The ratio of the gas density at high and low redshift can be assumed to scale as the ratio of the two virial densities, i.e., $\frac{\rho_{v,z=0.7}}{\rho_{v,z=0.2}} = \frac{M_{v,z=0.7}}{\left(R_{v,z=0.7}\right)^3} \times \frac{\left(R_{v,z=0.2}\right)^3}{M_{v,z=0.2}}$. In the case $M_{v,z=0.7} = M_{v,z=0.2}$, the density ratio becomes simply proportional to $\left(R_{v,z=0.2}/R_{v,z=0.7}\right)^3$. Specifically, considering both at low and high-z $M_v \simeq 1.0 \times 10^{15}$ M$_\odot$ and $\Delta M_v \simeq M_v/3$, the above equations give a ratio $\left(v_{i,z=0.7}/v_{i,z=0.2}\right)^3 \sim 1.5$ and $\rho_{v,z=0.7}/\rho_{v,z=0.2} \sim 2.2$. The

resulting ratio of turbulent energy flux derived at high and low redshift is then ~ 3.3.

The above calculation is approximate, because we only took kinematic effects and ΛCDM cosmology into account. We thus also use simulations in Cassano & Brunetti (2005) to calculate the injection of turbulence during simulated cluster merging histories, and derived the turbulent energy injected in the volume swept by the infalling subcluster. We found that in this case the distributions of the turbulent energy fluxes derived for clusters with $M_v \simeq 0.9 - 1.4 \times 10^{15}\, M_\odot$ in the two redshift ranges $0.2 - 0.3$ and $0.7 - 0.8$ differ by a factor of $\sim 3 - 4$, in a good agreement with the simpler derivation reported above.

Radiative lifetime and electrons acceleration in high-z clusters

In the paper we have assumed that $\eta_{\rm rel}$, i.e. the fraction of turbulent energy flux that is absorbed by relativistic electrons (Eq. 4.1), is constant with redshift. This depends on the energy budget of the population of re-accelerated seed electrons, and on the microphysics of the nonlinear interaction between turbulence and particles. The latter is assumed to be redshift-independent (e.g. Brunetti & Lazarian, 2007). Thus, a constant $\eta_{\rm rel}$ implies a similar energy budget of the seed electrons that are accumulated in high- and low-z ICM.

More specifically, we used Eq. 4.1 to infer a lower limit to the ratio of the magnetic field in high- and low-z radio halos, thus our conclusions may change in the case that clusters at higher redshift host a population of seed electrons with a much larger energy budget. In this section we show that this possibility is very unlikely, as the higher injection rate of electrons in the ICM expected from high-redshift sources is balanced by the stronger electron energy losses.

The budget of seed electrons that accumulate in the ICM can be estimated as $N_e \propto Q_e \times T_{\rm max}$ (with Q_e the injection rate and $T_{\rm max}$ the maximum electron lifetime). The lifetime of relativistic electrons in the ICM, which is determined by the energy losses due to Coulomb interaction with the thermal plasma and to Inverse Compton scattering with the CMB photons and synchrotron losses, can be expressed as (Brunetti & Jones, 2014):

$$T = 4 \left\{ \frac{1}{3} \tilde{\gamma} \beta_z + \frac{\tilde{n}}{\tilde{\gamma}} \left[1.2 + \frac{1}{75} \ln \left(\frac{\tilde{\gamma}}{\tilde{n}} \right) \right] \right\}^{-1} , \tag{4.8}$$

where we put $\tilde{\gamma} = \gamma/300$, $\tilde{n} = n/10^{-3}$, $\beta_z = \left(\frac{B}{3.2}\right)^2 + (1+z)^4$. Here, γ is the Lorentz factor, n the number density in cm^{-3} and B the magnetic field strength in μG. This lifetime increases with the energy γ of relativistic

electrons at lower energy, it reaches a maximum and then decreases as a function of γ.

The maximum of T is obtained for $\tilde{\gamma} \approx \sqrt{\frac{3\tilde{n}}{\beta_z}}$. For $B < B_{\rm CMB}$, it is determined by the combination of IC and Coulomb losses. Replacing this in Eq. 4.8 gives the typical lifetime of relativistic electrons that can be accumulated in the ICM on cluster lifetime and then re-accelerated during mergers:

$$T_{\rm max}\,[{\rm Gyr}] = 4\left\{\frac{\beta_z}{3}\sqrt{\frac{3\tilde{n}}{\beta_z}} + \tilde{n}\sqrt{\frac{\beta_z}{3\tilde{n}}}\right\}^{-1} . \quad (4.9)$$

Considering that between $z = 0.2$ and $z = 0.7$ the virial density (and hence the thermal gas density n) increases by a factor of ~ 2, the maximum lifetime ratio for electrons radiating at these two redshifts is ~ 2.7, considering $B \sim 1 - 2\ \mu$G.

Several sources can inject electrons in the ICM including AGN, galaxies (galactic winds, GW) and cosmological shocks. Most of the energy of the relativistic plasma of GW and shocks is in the form of supra-thermal and relativistic protons with only a negligible fraction in the form of electrons (e.g. Brunetti & Jones, 2014).

AGN are thought to be the dominant sources of relativistic electrons in the ICM (e.g. Brunetti & Jones, 2014); this hypothesis is also supported by recent LOFAR observations, where sources of fossil radio plasma from old AGN-electrons are commonly found in galaxy clusters (de Gasperin et al., 2017; Mandal et al., 2020). The injection rate of electrons from a number of AGN in clusters, $N_{\rm AGN}$, is $Q_e \sim N_{\rm AGN} n_{\rm rel} V/\Theta$, where $n_{\rm rel}$ is the number density of radio-emitting electrons in the jets and lobes, V is the volume of the radio plasma and Θ is the AGN life-time. The number density of radio-emitting electrons in the AGN lobes can be estimated assuming equipartition between particles and magnetic fields, i.e. $n_{\rm rel} \propto \sqrt{L_{\rm syn}/V}$, with $L_{\rm syn}$ the AGN synchrotron luminosity. This gives $Q_e \propto \sqrt{L_{\rm syn} V} N_{\rm AGN}/\Theta$. The linear size of radio galaxies is observed to decline with redshift, probably due to the higher density of the medium in which radio lobes and jets expand (Neeser et al., 1995; Blundell et al., 1999). Thus we attempt to account for the expected change of V with redshift assuming approximate pressure equilibrium of the lobes with the surrounding medium. This would imply $P_{\rm ICM} \propto n_{\rm rel} \propto \sqrt{L_{\rm syn}/V}$ and consequently $Q_e \propto L_{\rm syn} N_{\rm AGN}/(P_{\rm ICM}\Theta) \approx \rho_L (1+z)^3/(P_{\rm ICM}\Theta)$, where ρ_L is the luminosity density of radio AGN per comoving-volume. The luminosity density increases by a factor $\sim 2 - 2.5$ from $z \sim 0.2$ to $z \sim 0.7$ (Smolčić et al., 2017, their Fig. 5). The increase of $P_{\rm ICM}$ with redshift can be estimated using virial quantities, i.e. $P_{\rm ICM} \propto n_{\rm ICM} T_{\rm ICM} \propto \frac{M_v}{R_v^3}\frac{M_v}{R_v}$, implying that pressure increases by a factor ~ 2.5 from $z \sim 0.2$ to $z \sim 0.7$ for clusters with the same virial mass. We find that Q_e is only about 2-3 times larger in clusters at $z \sim 0.7$ if we assume that

the life-time of AGN does not change much with redshift. Combining this result with the maximum lifetime of the radiating electrons, that is ~ 2.7 times longer at lower redshift, suggests that the budget of seed electrons at low and high redshift is similar.

Seed electrons in the ICM can also be generated by the decay chain of inelastic proton-proton collisions (e.g. Brunetti & Lazarian, 2011; Pinzke et al., 2017). The importance of this channel depends on the energy budget of CR in the ICM, which is poorly known. A relevant contribution of re-accelerated secondary particles to radio halos is still allowed by current gamma-ray limits from FERMI-LAT (e.g. Brunetti et al., 2017). For this reason, we also compare the budget of secondary electrons accumulated in galaxy clusters at low and high redshift considering cosmological shocks as the main sources of relativistic protons. In this case, numerical simulations suggest the ratio of CR to thermal ICM pressures ($X = P_{\rm CR}/P_{\rm ICM}$) in high-$z$ clusters is generally smaller than that at low redshift (e.g. Vazza & Brüggen, 2014). The ratio of the energy budget of secondary electrons at high and low redshift can be approximately estimated as:

$$\frac{N_{e,z=0.7}}{N_{e,z=0.2}} \sim \frac{X_{z=0.7}}{X_{z=0.2}} \frac{n_{{\rm ICM},z=0.7} P_{{\rm ICM},z=0.7}}{n_{{\rm ICM},z=0.2} P_{{\rm ICM},z=0.2}} \frac{T_{{\rm max},z=0.7}}{T_{{\rm max},z=0.2}} , \tag{4.10}$$

implying $N_{e,z=0.7}/N_{e,z=0.2} \sim 0.4 - 1.8$ if we assume typical CR pressure ratios measured in simulations, i.e. $\sim 0.2 - 1$ (Vazza et al., 2012b; Vazza & Brüggen, 2014, Figs. 14 and Fig. 12 respectively), and the ratios between physical quantities as derived above: $T_{{\rm max},z=0.7}/T_{{\rm max},z=0.2} \sim 1/2.7$, $P_{{\rm ICM},z=0.7}/P_{{\rm ICM},z=0.2} \sim 2.5$ and $n_{{\rm ICM},z=0.7}/n_{{\rm ICM},z=0.2} \sim 2$. Similarly to the case of AGN, this implies that the budget of secondary particles that is available at higher redshift is very similar to that at low redshift.

Reynolds number estimation

In Figure 4.3b we have used a simple model of magnetic field amplification to infer combined constraints on the initial magnetic field and on the Reynolds number. We follow the method as outlined in Beresnyak (2012). We assume that the amplification initially operates in a kinematic regime, where the magnetic field grows exponentially with time:

$$B^2(t) \sim B_0^2 \exp\left(t\,\Gamma\right) , \tag{4.11}$$

where the time-scale of the magnetic growth is $\Gamma^{-1} \sim 30 L_d/\delta v_d$. This depends on the turbulent eddy turnover time at the viscous dissipation scale, $L_d \sim L_{\rm inj}\,{\rm Re}^{-3/4}$, $\delta v_d \sim v_t (L_d/L_{\rm inj})^{1/3}$. The factor ~ 30 is derived from simulations (Cho, 2014; Beresnyak & Miniati, 2016), and accounts for the less effective stretching of the field lines due to the turbulent diffusion. When the

magnetic and the kinetic energy densities become comparable at the viscous dissipation scale ($B(t)^2/8\pi \sim 1/2\rho\delta v_d^2$), the turbulent dynamo transits to a phase where the magnetic field grows linearly with time. This phase is known as the non-linear regime because the magnetic field (Reynolds stress) becomes dynamically important. From Eq. 4.11, this transition occurs at a time:

$$t_* \sim 60 \frac{L_{\rm inj}}{v_t} {\rm Re}^{-1/2} \ln\left(\frac{B_*}{B_0}\right) \tag{4.12}$$

where $B_* \sim \sqrt{4\pi\rho}\, v_t {\rm Re}^{-1/4}$. According to simulations, in the non-linear regime, i.e. for time $t \geq t_*$, we assume that a constant fraction of the turbulent kinetic energy flux, η_B, is channeled into magnetic field energy ($\eta_B = 0.05$, Beresnyak, 2012). Therefore, the evolution of the magnetic field with time is:

$$B^2(t) \sim B_*^2 + 4\pi \frac{\rho v_t^3}{L_{\rm inj}} \eta_B (t - t_*)\,. \tag{4.13}$$

In the calculations shown in Figure 4.3b, we assume a continuous injection of turbulence with $v_t = 500$ km s^{-1} at the injection scale $L_{\rm inj} = 1$ Mpc, and $n = \rho/m_p = 3\times10^{-3}$ cm^{-3} (with m_p the proton mass). We note that a situation of continuous injection of turbulence with these parameters is appropriate for a dynamically active and massive cluster (Dolag et al., 2005; Donnert et al., 2018; Hitomi Collaboration et al., 2018; Markevitch & Vikhlinin, 2007) and consequently calculations would overestimate the magnetic field strength if extrapolated for a time scale that is much larger than that of a typical merger.

An important parameter in the model is the time when the turbulent dynamo starts, as it fixes the time available for magnetic field amplification up to the epoch of observation. Here, we assume that the turbulent dynamo starts when the clusters have formed a quarter of their mass. This implies that the time available for the amplification is of about 3.7 Gyr (Fakhouri et al., 2010; Giocoli et al., 2012). Assuming a turbulent velocity of $v_t = 500$ km s^{-1} at an earlier stage in the cluster life-time is optimistic, as the cluster would be too small. Since the turbulent energy flux is proportional to v_t^3, the effect of much weaker turbulence at earlier epochs is not relevant for the magnetic field evolution. Conversely, if we assume that the dynamo started later in the cluster life-time, e.g. when it has assembled half of its mass, it results in more stringent Reynolds numbers, since the time available for the amplification is shorter (about 2.7 Gyr). Lower turbulent velocities and lower number densities would imply higher values of the Reynolds number. On the other hand, higher turbulent velocities would imply a smaller value of Re. However, even if we consider $v_t = 800$ km s^{-1} (Dolag et al., 2005; Donnert et al., 2018), i.e. the case of a large turbulent pressure of about 30–40% the ICM pressure, we obtain Reynolds numbers

that are only three times smaller than the case with v_t = 500 km s^{-1}. We also mention that in real clusters turbulence is induced in a medium that is highly stratified due to gravity (Roh et al., 2019). In this case, the transport of magnetised turbulent eddies toward the outskirts could make the turbulent dynamo slightly less efficient than in our model, implying that our constraints on the Reynolds number are conservative.

4.2. Supplementary

Physical properties of the galaxy clusters in the sample

Here, we report the properties of the galaxy clusters selected from the *Planck* sample (Table 4.2).

LOFAR images

In this section we present the LOFAR full resolution source-subtracted images of the clusters in our sample (Figure 4.6). The radio contours of the subtracted radio galaxies overlaid, starting from $3\sigma_{\rm rms}$, with $\sigma_{\rm rms}$ the noise of the full-resolution uv-cut map, spaced by a factor of 2. The dashed contours display the $-3\sigma_{\rm rms}$ contour level.

Below we provide a brief description of the galaxy clusters (ObsIDs list is reported in Table 4.3).

- PSZ2 G045.87+57.70 (z = 0.611) shows extended diffuse radio emission in the north-south direction, which is unresolved in the east-west direction. For this reason, and since it is not located in the cluster center, we classify this emission as "uncertain". The X-ray emission also looks elongated in the north-south direction.

- PSZ2 G070.89+49.26 (z = 0.610) is actually a double cluster (Planck Collaboration et al., 2015). In both systems, there is no evidence of diffuse radio emission (see Figure 4.4).

- PSZ2 G084.10+58.72 (z = 0.731) does not show clear presence of extended diffuse emission in the full resolution image. The X-ray emission suggests a dynamically disturbed system.

- An extended, probably foreground, radio galaxy contaminates the radio emission from PSZ2 G086.28+74.76 (z = 0.699). We cannot classify this cluster hosting diffuse radio emission. No X-ray observations are available.

- PSZ2 G086.93+53.18 (z = 0.675) is the faintest candidate halos in our sample. We find hints of diffuse radio emission on the $2\sigma_{\rm rms}$

Table 4.2: List of galaxy clusters from Planck SZ Catalog with DEC $\geq 20°$ and $z \geq 0.6$

PSZ name	z	RA_{J2000} [deg]	DEC_{J2000} [deg]	$M_{SZ,500}$ [10^{14} $M_\odot$]	LOFAR	*Chandra*	*XMM*	Ref.
PSZ2G032.31+66.07	0.609	219.35404	+24.3986	5.6 ± 0.8				(a,g,i)
PSZ2G045.87+57.70	0.611	229.58737	+29.46957	7.0 ± 0.7	✓		✓	(a)
PSZ2G066.34+26.14	0.630	270.277	+39.86853	4.8 ± 0.7				(a,g,i)
PSZ2G069.39+68.05	0.762	215.40979	+38.35494	–				(a,d,g)
PSZ2G070.89+49.26	0.610	239.21558	+44.63012	6.5 ± 0.7	✓		✓	(a)
PSZ2G073.31+67.52	0.609	215.16250	+39.91500	6.7 ± 0.6			✓	(a)
PSZ2G084.10+58.72	0.731	222.25554	+48.55556	5.4 ± 0.6	✓	✓	✓	(a)
PSZ2G085.95+25.23	0.782	277.6164	+56.8823	5.4 ± 0.6				(a,b,i)
PSZ2G086.28+74.76	0.699	204.47446	+38.90189	$5.3^{+0.7}_{-0.8}$	✓			(a,g,i)
PSZ2G086.93+53.18	0.675	228.50446	+52.81074	5.4 ± 0.5	✓	✓	✓	(a)
PSZ2G087.39+50.92	0.748	231.63821	+54.15210	$5.2^{+0.5}_{-0.6}$	✓		✓	(a)
PSZ2G088.98+55.07	0.702	224.74384	+52.81730	4.9 ± 0.6	✓	✓	✓	(a)
PSZ2G089.39+69.36	0.680	208.43748	+43.48476	5.7 ± 0.7	✓			(a)
PSZ2G091.83+26.11	0.822	277.78430	+62.24770	7.4 ± 0.4	✓	✓	✓	(a,b)
PSZ2G092.69+59.92	0.848	216.65041	+51.26417	4.5 ± 0.5	✓	✓	✓	(a,d,i)
PSZ2G097.52+51.70	0.700	223.8588	+58.85514	5.2 ± 0.5	✓		✓	(a)
PSZ2G099.86+58.45	0.616	213.6909	+54.78029	6.8 ± 0.5	✓		✓	(a,e,f)
PSZ2G100.22+33.81	0.620	258.43971	+69.36335	–				(a,g)
PSZ2G104.74+40.42	0.690	236.6082	+69.95975	$4.3^{+0.5}_{-0.6}$	✓			(a,c)
PSZ2G106.15+25.75	0.630	284.25043	+74.93208	4.6 ± 0.7				(a,h)
PSZ2G108.27+48.66	0.674	52.79720	+65.65932	4.9 ± 0.5				(a,c)
PSZ2G126.28+65.62	0.820	190.5975	+51.43944	5.0 ± 0.7	✓			(a,d,i)
PSZ2G126.57+51.61	0.815	187.4492	+65.35361	5.8 ± 0.6				(a,d,i)
PSZ2G127.01+26.21	0.630	89.6057	+86.2544	$7.3^{+0.8}_{-0.9}$	✓	✓		(a)
PSZ2G139.00+50.92	0.600	170.070701	+63.24996	$4.6^{+0.7}_{-0.8}$	✓			(a,g,i)
PSZ2G141.77+14.19	0.830	70.27167	+68.22275	7.7 ± 0.9	✓	✓		(a,h)
PSZ2G141.98+69.31	0.714	183.16929	+46.35641	$4.1^{+0.9}_{-0.9}$	✓			(a,g,i)
PLCKG147.3–16.6	0.645	44.105898	+40.290140	6.3 ± 0.4	✓		✓	(a,b,j)
PSZ2G147.88+53.24	0.600	164.37923	+57.99591	6.5 ± 0.6	✓			(a)
PSZ2G160.83+81.66	0.888	186.74267	+33.54682	$5.7^{+0.6}_{-0.7}$	✓	✓	✓	(a)

References: (a) Planck Collaboration et al. (2016); (b) Amodeo et al. (2018), (c) Barrena et al. (2018), (d) Burenin et al. (2018), (e) Cassano et al. (2019), (f) Sereno et al. (2018), (g) Streblyanska et al. (2018), (h) van der Burg et al. (2016), (i) Zohren et al. (2019), (j) van Weeren et al. (2014).

level, located southward of the BCG. The X-ray emission is spherically symmetric within the $R = 0.5R_{500}$ region.

- PSZ2 G087.39+50.92 ($z = 0.748$) does not show extended radio emission. The X-ray image suggests this is a dynamically relaxed system.

- PSZ2 G089.39+69.36 ($z = 0.680$) hosts a bright radio halo with a size of about 1 Mpc. No X-ray observations are available for this cluster.

- PSZ2 G091.83+26.11 ($z = 0.822$) hosts the brightest radio halo in our sample ($S_{144\mathrm{MHz}} = 84.3 \pm 12.7$ mJy). Moreover, it also hosts an elongated 1.2 Mpc arc-like radio source. No clear optical counterparts is found for this source. The brightest region of this arc is also visible in a short Very Large Array (VLA) observation, which also allowed us to define the relic region for the flux density measurements (see the blue polygon in Figure 4.7). Future spectral index and polarization studies would help to verify the different contributions of the halos and relic. Combining our LOFAR flux density measurements with that of the VLA yields an integrated spectral index of $\alpha \sim -1.6$ (also see the following Section). The steep spectral index, the lack of clear optical counterparts and the elongated shape, strongly suggest we are observing a radio relic. Shallow X-ray observations also show disturbed thermal emission, elongated in the north-south direction, suggesting that the cluster is in a merging state (second panel in Figure 4.2). The radio relic is located parallel to the putative merger axis, and not perpendicularly to it as it is usually observed in low-redshift systems. This suggests a merger that is more complex than a head-on binary merger.

- PSZ2 G092.69+59.92 ($z = 0.848$) does not show extended radio emission. The dynamical state of this cluster is unclear from the X-ray image.

- The radio halo in PSZ2 G099.86+58.45 ($z = 0.616$) was recently studied (Cassano et al., 2019), combining LOFAR, VLA and *XMM-Newton* observations. The cluster is thought to undergo a merger event. Additionally, it has been claimed (Sereno et al., 2018) that this cluster is located in a particularly high-density environment, which might have favored the formation of the halo.

- PSZ2 G104.74+40.42 ($z = 0.690$) shows hints of presence of extended radio emission. After subtracting the flux density of the radio galaxies in the cluster volume, the resulting diffuse radio emission result to be $S_{144\mathrm{MHz}} < 5\Delta S$, hence it is classified as "uncertain" detection. No X-ray observations are available.

- Although the radio emission is dominated by three radio galaxies, PSZ2 G126.28+65.62 (z = 0.820) shows evidence of diffuse radio emission, spanning a region of about 800 kpc. No X-ray observations are available.
- All the radio emission detected in PSZ2 G127.01+26.21 (z = 0.630) is associated with the radio galaxies. The X-ray emission is peaked on the BCG, appearing elongated in the north-south direction.
- A small double-lobed radio galaxy is observed in the center of PSZ2 G139.00+50.92, without hints of diffuse emission. No X-ray observations are available.
- The radio halo in PSZ2 G141.77+14.19 extends over 600 kpc. The X-ray emission appears very disturbed and elongated in the northwest-southeast direction.
- PSZ2 G141.98+69.31 (z = 0.714) does not show extended radio emission. No X-ray observations are available.
- Diffuse radio emission in PLCKG147.3–16.6 (z = 0.645) extends in the east-west direction over 800 kpc. Optical and X-ray data suggest the cluster is undergoing a merger event. The radio halo was earlier discovered using GMRT observations (van Weeren et al., 2014). Using the GMRT and LOFAR halo flux densities, we calculate an integrated spectral index $\alpha = -0.77 \pm 0.15$. This value is flatter than what we assume for the other radio halos in our sample, but it is consistent, within the uncertainties, with other literature radio halos (Feretti et al., 2012). Further studies on the spectral index of this source are however needed.
- The radio emission in PSZ2 G147.88+53.24 (z = 0.600) has a largest size of about 600 kpc. The emission encompasses the BCG in the south-west direction. No X-ray observations are available for this cluster.
- PSZ2 G160.83+81.66, at z = 0.888, represents the highest redshift object of our sample. Diffuse radio emission is detected extending over 700 kpc centered around the central BCG. The radio emission follows the thermal gas emission (see last panel in Figure 4.2). This is the most distant radio halo discovered so far. Deep X-ray observations (Maughan et al., 2007) suggest this cluster has a relaxed morphology (see also last panel in Figure 4.2). However, no signs of central cooling have been found from an X-ray temperature analysis, suggesting a possible earlier merger event (Maughan et al., 2007). In agreement with this, a weak lensing analysis revealed a bimodal mass distribution (Jee & Tyson, 2009).

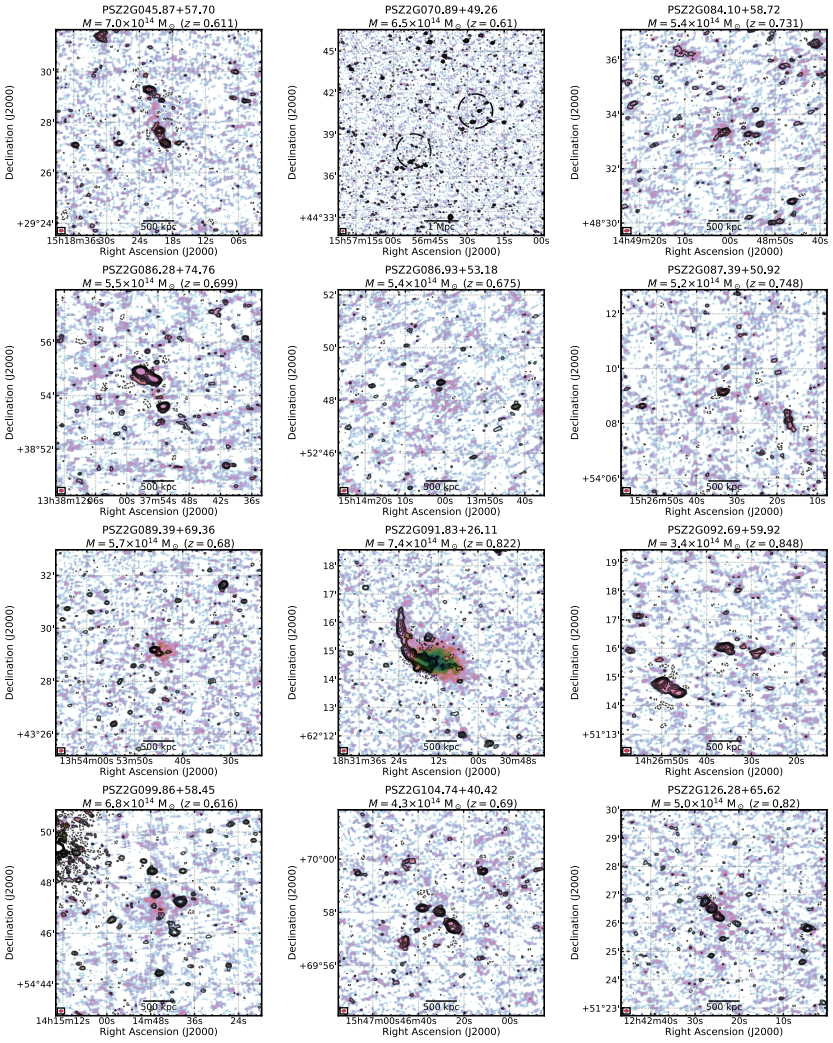

Figure 4.6: Observed diffuse radio emission in our high-z galaxy cluster sample. In colorscale we show the full-resolution LOFAR images of the clusters in our sample after the subtraction of the compact sources. Radio contours show the subtracted compact sources, at the same resolution. The contour levels are drawn at $2\sigma_{\rm rms} \times [-1, 1, 2, 4, \dots]$, with $\sigma_{\rm rms}$ the noise level of the full-resolution uv-cut image (with the short-dashed line displaying the negative contour). In the header of each image, the galaxy cluster name, mass and redshift are reported. The dashed black circle in each map shows the $R = 0.5R_{\rm SZ,500}$ region, obtained from $M_{\rm SZ,500}$.

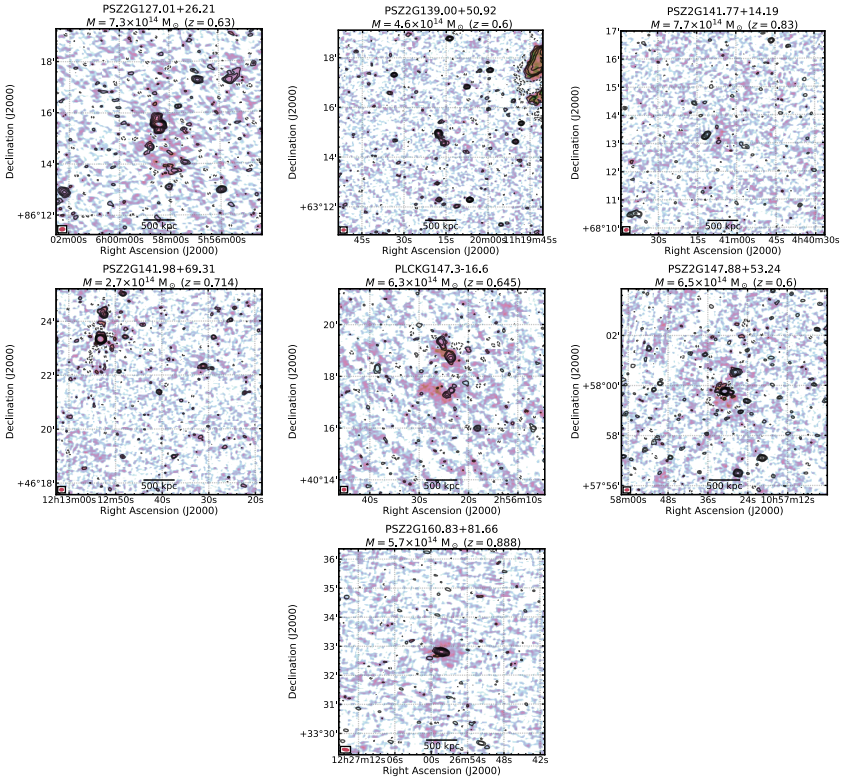

Figure 4.6: Continued.

Additional flux density measurements

In Table 4.1 we reported the flux density measurements and the largest linear size of the candidate radio halos obtained following the $2\sigma_{\rm rms}$ radio contour in the low-resolution source-subtracted image. Here, we report the same analysis but following the $3\sigma_{\rm rms}$ radio contour (see Table 4.4). Moreover, we also provide flux density measurements from the low-resolution source-subtracted images, following both the 2 and $3\sigma_{\rm rms}$ radio contours. The uncertainty on the flux densities are calculated as Equation 2 but, in this case, the term $\sigma^2_{\rm sub}$ refers to the uncertainty due to the source subtraction in the *uv* plane, i.e. a fraction (about 3%) of the total flux of the subtracted radio galaxies (see Cassano et al., 2013; Hoang et al., 2017).

Table 4.3: ObsIDs list of the LOFAR observations.

PSZ name	ObsID(s)
PSZ2G045.87+57.70	P230+27, P228+30, P231+30
PSZ2G070.89+49.26	P236+45, P240+45
PSZ2G084.10+58.72	P221+47,P223+50,P225+47
PSZ2G086.28+74.76	P203+37, P204+40
PSZ2G086.93+53.18	P227+55, P227+53, P231+53
PSZ2G089.39+69.36	P207+45, P209+42
PSZ2G091.83+26.11	P275+60, P281+63, P275+63, P280+60
PSZ2G092.69+59.92	P214+52, P215+50, P219+52, P219+50
PSZ2G099.86+58.45	P209+55, P214+55
PSZ2G104.74+40.42	P240+70, P232+70
PSZ2G126.28+65.62	P33Hetdex08, P29Hetdex19, P30Hetdex06
PSZ2G127.01+26.21	P098+84, P113+87, P066+87
PSZ2G139.00+50.92	P168+62, P168+65
PSZ2G141.77+14.19	P075+69, P072+67, P068+69
PSZ2G141.98+69.31	P20Hetdex17, P23Hetdex20, P19Hetdex17
PLCKG147.3–16.6	P044+39, P045+41, P042+41
PSZ2G147.88+53.24	P166+60, P165+57
PSZ2G160.83+81.66	P185+35, P188+35, P188+32, P185+32

Additional radio maps and integrated spectral index for PSZ2 G091.83+26.11

PSZ2 G091.83+26.11 was observed with the Very Large Array (VLA), in the 1–2 GHz frequency band, in the B-array configuration on the 22nd of March 2015 (project code: 15A-270). The total time on source is about 40 minutes. Standard VLA data reduction (Di Gennaro et al., 2018) has been performed on the dataset with `CASA v5.3` (McMullin et al., 2007). Applied corrections included the antenna delays, bandpass, cross-hand delays, and polarisation leakage and angles using the primary calibrators 3C286 and 3C147. These calibration solutions were applied to the target, and self-calibration was performed to refine the amplitudes and phases. The final image was produced using w-projection (Cornwell et al., 2005, 2008), Briggs weighting with `robust=0` and `nterms=3` (Rau & Cornwell, 2011). The correction for the primary beam attenuation has also been applied. The final image resolution is $3.8'' \times 3.0''$, with a noise of $\sigma_{\rm rms} = 50.7$ μJy beam^{-1}. Only the brightest part of the relic is visible in this observation (Supplementary Figure 3). We measured a radio flux density of $S_{1.5\rm GHz} \sim 5.5$ mJy. Combined LOFAR-VLA images yields an integrated spectral index of $\alpha \sim -1.6$. The lack of short baselines and short on-source integration time,

Table 4.4: Integrated flux density and radio luminosity of the galaxy clusters observed with LOFAR. Column 1: *Planck* cluster name. Column 2: Cluster redshift. Column 3: Largest linear size (LLS), following the 2 and $3\sigma_{\rm rms}$ radio contours. Columns 4 and 5: The integrated flux density and radio luminosity measurements, following the $2\sigma_{\rm rms}$ and $3\sigma_{\rm rms}$ contours (from Figure 4.4), and, for both, the values using the flux-subtraction (see Method) and the *uv*-subtraction (see above) strategies.

Planck (PSZ) name	z	LLS [Mpc]		Classification	$S_{144\rm MHz}$ [mJy]				$P_{1.4\rm GHz}$ [10^{24} W Hz^{-1}]			
		$2\sigma_{\rm rms}$	$3\sigma_{\rm rms}$		$2\sigma_{\rm rms}$		$3\sigma_{\rm rms}$		$2\sigma_{\rm rms}$		$3\sigma_{\rm rms}$	
					flux sub	*uv*-sub	flux sub	*uv*-sub	flux sub	*uv*-sub	flux sub	*uv*-sub
PSZ2G045.87+57.70	0.611	–	–	Uncertain	–	–	–	–	–	–	–	–
PSZ2G070.89+49.26	0.610	–	–	–	–	–	–	–	–	–	–	–
PSZ2G084.10+58.72	0.731	–	–	Uncertain	–	–	–	–	–	–	–	–
PSZ2G086.28+74.76	0.699	–	–	Uncertain	–	–	–	–	–	–	–	–
PSZ2G086.93+53.18	0.675	0.5	0.3	Halo/Uncertain	7.2 ± 1.5	7.9 ± 1.6	4.3 ± 0.8	5.2 ± 1.0	0.7 ± 0.4	0.8 ± 0.5	0.5 ± 0.2	0.5 ± 0.3
PSZ2G087.39+50.92	0.748	–	–	–	–	–	–	–	–	–	–	–
PSZ2G089.39+69.36	0.680	1.0	0.9	Halo	12.5 ± 1.9	11.9 ± 1.7	10.3 ± 1.5	10.1 ± 1.5	1.3 ± 0.7	1.1 ± 0.6	1.0 ± 0.6	0.9 ± 0.5
PSZ2G091.83+26.11	0.822	1.2	1.2	Halo	84.3 ± 12.7	73.0 ± 9.0	83.9 ± 11.4	72.8 ± 9.0	13.8 ± 8.4	12.4 ± 5.5	12.6 ± 5.6	11.8 ± 4.0
		1.2		Relic	259.4 ± 38.9	–	–	–	–	–	–	–
PSZ2G092.69+59.92	0.848		–	–	–	–	–	–	–	–	–	–
PSZ2G099.86+58.45	0.616	1.2	1.0	Halo	27.8 ± 4.3	21.5 ± 3.6	21.0 ± 3.2	17.6 ± 3.0	2.2 ± 1.3	1.7 ± 0.9	1.6 ± 1.0	1.4 ± 0.9
PSZ2G104.74+40.42	0.690	–	–	Uncertain	–	–	–	–	–	–	–	–
PSZ2G126.28+65.62	0.820	0.8	0.8	Halo	8.8 ± 1.7	9.2 ± 1.8	5.5 ± 1.1	6.3 ± 1.2	1.4 ± 0.6	1.7 ± 0.9	0.9 ± 0.4	1.4 ± 0.9
PSZ2G127.01+26.21	0.630	–	–	Uncertain	–	–						
PSZ2G139.00+50.92	0.600	–	–	–	–	–	–	–	–	–	–	–
PSZ2G141.77+14.19	0.830	0.6	0.5	Halo	8.8 ± 1.4	9.0 ± 1.6	4.7 ± 0.8	6.4 ± 1.2	1.4 ± 0.7	1.6 ± 0.7	0.7 ± 0.4	1.1 ± 0.6
PSZ2G141.98+69.31	0.714	–	–	–	–	–	–	–	–	–	–	–
PLCKG147.3–16.6	0.645	0.8	0.8	Halo	22.5 ± 3.7	23.2 ± 3.9	19.0 ± 3.0	19.4 ± 3.8	6.4 ± 3.4	6.7 ± 2.7	4.9 ± 1.7	5.9 ± 2.0
PSZ2G147.88+53.24	0.600	0.6	0.6	Halo	14.4 ± 2.3	11.8 ± 2.3	11.1 ± 1.7	10.0 ± 2.1	0.9 ± 0.5	0.7 ± 0.5	0.8 ± 0.4	0.8 ± 0.6
PSZ2G160.83+81.66	0.888	0.7	0.5	Halo	13.0 ± 2.1	10.6 ± 2.0	10.2 ± 1.6	7.9 ± 1.6	2.7 ± 1.5	2.2 ± 1.1	1.9 ± 1.0	1.7 ± 0.6

means that the radio halo cannot be detected.

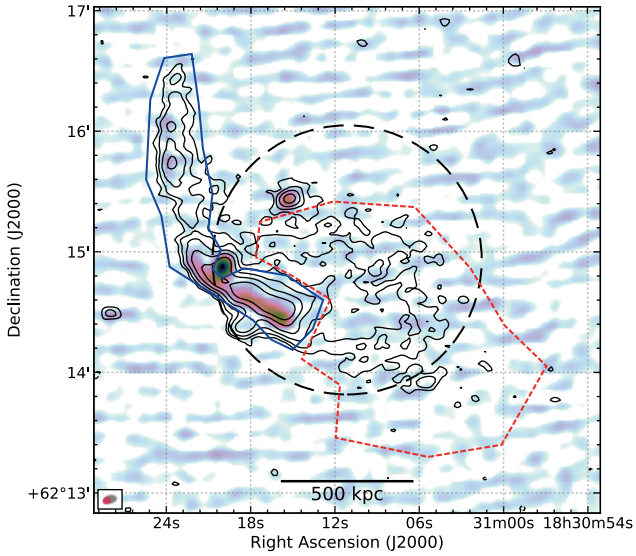

Figure 4.7: VLA-LOFAR comparison of PSZ2G091.83+26.11. In colorscale we show the 1–2 GHz B-array VLA radio image of the cluster. The full-resolution LOFAR radio contours are displayed at $3\sigma_{\rm rms} \times [-1, 1, 2, 4, \dots]$ level, with $\sigma_{\rm rms}$ the map noise and negative contours displayed with the short-dashed line, as comparison. The VLA and LOFAR beams are displayed in the bottom left corner, in pink and black respectively. The blue and red boxes show the regions where the flux densities were extracted, for the relic and the halo respectively.

X-ray observations and images

Here we list the summary (Supplementary Table 4.5) of the clusters with X-ray observations. For those clusters which had both *Chandra* and *XMM-Newton* observations, we only show the best case, i.e., a compromise between high resolution and exposure time.

Table 4.5: Supplementary Table 4: ObsIDs list of the X-ray observations.

PSZ name	Satellite	ObsID(s)	Total exposure time [ks]
PSZ2G045.87+57.70	*XMM-Newton*	0693661101	32
PSZ2G070.89+49.26	*XMM-Newton*	0693661301	50
PSZ2G084.10+58.72	*XMM-Newton*	783880901	86
PSZ2G086.93+53.18	*XMM-Newton*	0783880701	81
PSZ2G087.39+50.92	*XMM-Newton*	0783881201	22
PSZ2G091.83+26.11	*Chandra*	18285	23
PSZ2G092.69+59.92	*XMM-Newton*	0783880401 0783881901	107
PSZ2G099.86+58.45	*XMM-Newton*	0693660601 0693662701 0723780301	63
PSZ2G127.01+26.21	*Chandra*	18286	16
PSZ2G141.77+14.19	*Chandra*	18289	21
PLCKG147.3–16.6	*XMM-Newton*	0679181301	10
PSZ2G160.83+81.66	*Chandra*	3180 5014	67

Acknowledgements: The authors thank C. Giocoli and his team for the discussion on the cosmological derivations in the manuscript. This manuscript is based on data obtained with the International LOFAR Telescope (ILT). LOFAR (van Haarlem et al. 2013) is the Low Frequency Array designed and constructed by ASTRON. It has observing, data processing, and data storage facilities in several countries, which are owned by various parties (each with their own funding sources), and which are collectively operated by the ILT foundation under a joint scientific policy. The ILT resources have benefited from the following recent major funding sources: CNRS-INSU, Observatoire de Paris and Université d'Orléans, France; BMBF, MIWF-NRW, MPG, Germany; Science Foundation Ireland (SFI), Department of Business, Enterprise and Innovation (DBEI), Ireland; NWO, The Netherlands; The Science and Technology Facilities Council, UK; Ministry of Science and Higher Education, Poland; The Istituto Nazionale di Astrofisica (INAF), Italy. This research made use of the Dutch national e-infrastructure with support of the SURF Cooperative (e-infra 180169) and the LOFAR e-infra group. The Jülich LOFAR Long Term Archive and the German LOFAR network are both coordinated and operated by the Jülich Supercomputing Centre (JSC), and computing resources on the supercomputer JUWELS at JSC were provided by the Gauss Centre for Supercomputing e.V. (grant CHTB00) through the John von Neumann Institute for Computing (NIC). This research made use of the University of Hertfordshire high-performance computing facility and the LOFAR-UK computing facility located at the University of Hertfordshire and supported by STFC [ST/P000096/1], and of the Italian LOFAR IT computing infrastructure supported and operated by INAF, and by the Physics Department of Turin university (under an agreement with Consorzio Interuniversitario per la Fisica Spaziale) at the C3S Supercomputing Centre, Italy. The National Radio Astronomy Observatory is a facility of the National Science Foundation operated under cooperative agreement by Associated Universities, Inc. This work is based on observations obtained with XMM–Newton, an ESA science mission with instruments and contributions directly funded by ESA Member States and NASA. The scientific results reported in this manuscript are based in part on data obtained from the Chandra Data Archive. The Pan-STARRS1 Surveys (PS1) and the PS1 public science archive have been made possible through contributions by the Institute for Astronomy, the University of Hawaii, the Pan-STARRS Project Office, the Max-Planck Society and its participating institutes, the Max Planck Institute for Astronomy, Heidelberg and the Max Planck Institute for Extraterrestrial Physics, Garching, The Johns Hopkins University, Durham University, the University of Edinburgh, the Queen's University Belfast, the Harvard-Smithsonian Center for Astrophysics, the Las Cumbres Observatory Global Telescope Network Incorporated, the National Central University of Taiwan, the Space Telescope Science Institute, the National Aeronautics and Space Administration under Grant No. NNX08AR22G issued through the Planetary

Science Division of the NASA Science Mission Directorate, the National Science Foundation Grant No. AST-1238877, the University of Maryland, Eotvos Lorand University (ELTE), the Los Alamos National Laboratory, and the Gordon and Betty Moore Foundation. G.D.G. and R.J.v.W. acknowledge support from the ERC Starting Grant ClusterWeb 804208. G.B., R.C., F.G., M.R. acknowledge support from INAF through the mainstream project "Galaxy clusters science with LOFAR". A.Bot. and R.J.v.W. acknowledge support from the VIDI research programme with project number 639.042.729, which is financed by the Netherlands Organisation for Scientific Research (NWO). H.J.A.R. acknowledge support from the ERC Advanced Investigator programme NewClusters 32127. A. Bon. acknowledges support from the ERC Stg "DRANOEL" no. 714245 and from the MIUR grant FARE "SMS".